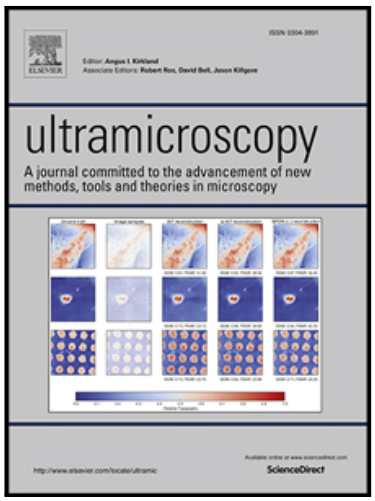

An inelastic multislice simulation method incorporating plasmon energy losses

BG Mendis

PII: S0304-3991(19)30162-7
DOI: https://doi.org/10.1016/j.ultramic.2019.112816
Article Number: 112816
Reference: ULTRAM 112816

To appear in: *Ultramicroscopy*

Received date: 9 May 2019
Revised date: 29 June 2019
Accepted date: 20 July 2019

Please cite this article as: BG Mendis , An inelastic multislice simulation method incorporating plasmon energy losses, *Ultramicroscopy* (2019), doi: https://doi.org/10.1016/j.ultramic.2019.112816

Highlights

- Plasmon losses are included in multislice simulations.
- Monte Carlo methods are used to estimate plasmon scattering lengths and angles.
- Simulations reproduce the trends observed in energy filtered, [110]-Si CBED patterns.
- Plasmon scattering is also found to lower the HAADF intensity from atom columns due to weaker channeling.

An inelastic multislice simulation method incorporating plasmon energy losses

BG Mendis
Dept of Physics, Durham University, South Road, Durham, DH1 3LE, UK

Abstract

Quantitative electron microscopy requires accurate simulation methods that take into account both elastic and inelastic scattering of the high energy electrons within the specimen. Here a method to combine plasmon excitations, the dominant energy loss mechanism in a solid, with conventional frozen phonon, multislice simulations is presented. The Monte Carlo based method estimates the plasmon scattering path length and scattering angle using random numbers and modifies the transmission and propagator functions in the multislice calculation accordingly. Comparison of energy filtered, convergent beam electron diffraction patterns in [110]-Si show good agreement between simulation and experiment. Simulations also show that plasmon excitation decreases the high angle annular dark field signal from atom columns, due to the plasmon scattering angle suppressing electron beam channeling along the atom columns. The effect on resolution and peak-to-background ratio of the atom columns is however small.

Keywords: multislice, frozen phonon, plasmons, convergent beam electron diffraction, high angle annular dark field

1. Introduction

The importance of thermal diffuse scattering (TDS) to correctly interpret diffraction contrast images of defects [1] and atomic column contrast of high angle annular dark field (HAADF) images [2-3] is well known. In Bloch wave theory TDS is modelled via an 'optical' potential [1], where the imaginary part of the complex electrostatic potential describes the anomalous absorption due to inelastic scattering. This is however a phenomenological approach where the TDS electrons are effectively removed from the purely elastic scattering calculation. Hence, although computationally efficient, a serious weakness of the optical potential method is that the electron flux is not conserved. This limitation is however overcome in the frozen phonon model [4-5]. Here it is assumed that within the short time it takes the high energy incident electron to traverse the thin foil specimen the atoms are effectively frozen in space, such that their displacements from the equilibrium positions are governed by the phonon modes of the material. Multislice simulations [6-7] are performed for different atomic configurations and the results incoherently summed to give a statistical average. The frozen phonon method ignores the small phonon energy loss and is therefore, strictly speaking, a quasi-elastic scattering calculation. It can be shown to be equivalent to the full quantum mechanical treatment [8] involving both elastic and inelastic scattering provided certain conditions are satisfied [9-10]. Furthermore, the versatility of the frozen phonon method makes it an ideal simulation tool for a wide range of applications.

Fast computation speeds enabled by a graphics processing unit (GPU) means that frozen phonon multislice simulations can now been performed on supercells that contain over a million atoms [11-12]. Examples include HAADF images obtained from liquid cell microscopy [13], where the presence of Si_3N_4 windows and a fluid layer can result in specimen thicknesses of several hundred nanometres, particularly in the central region where bulging of the Si_3N_4 windows takes place [14]. For specimens this thick it is not sufficient to consider only TDS; other forms of inelastic scattering must also be taken into account. Single electron, core shell ionisation losses are modelled using quantum mechanics [15] and can be incorporated within a modified multislice algorithm [16-18]. However, the energy loss spectrum for a thin-foil specimen indicates bulk plasmons to be the dominant energy loss feature, while core loss edges are relatively weaker [19]. Since a plasmon is a collective oscillation of valence electrons calculation of its transition matrix element is a many-body problem. This considerably increases the complexity of the underlying physics, making it difficult to include plasmon losses even in inelastic multislice simulations. Nevertheless it is clear that an accurate description of electron beam scattering must at least include plasmon losses, since it is the most probable energy loss mechanism.

Here we develop an inelastic multislice simulation that includes plasmon losses. The method is inspired by the Monte Carlo technique [20], which is extremely adept at combining both elastic and inelastic scattering, but which overlooks the wave nature of the high energy electron, and therefore cannot reproduce important effects such as electron beam channeling within a crystal. By merging elements of the Monte Carlo method with multislice the shortcomings of each technique can be mitigated. In particular random numbers are used to estimate the scattering path length and scattering angle for plasmon excitation. The random number distributions are such that the plasmon mean free path and characteristic scattering angle [19, 21] are reproduced. Within the multislice framework plasmon excitation can be shown to modify the transmission and propagator functions to that of a tilted beam [22], with the degree of tilt being determined by the particular scattering angle. By incoherently summing the results for different combinations of scattering depths and angles a statistically averaged result is obtained. Frozen phonons are also included so that the multislice simulations take into account both TDS and plasmon scattering. Previous attempts in the literature [23-24] have used perturbation methods to include plasmon losses in multislice. This results in an 'effective' potential and hence a modified transmission function, although the propagator function is unchanged. The Monte Carlo method however captures more of the underlying physics by modifying both transmission and propagator functions. The mathematical procedure for modelling plasmon losses is described in section 2, while a comparison of experimental results with simulation is presented in section 4.

2. Background theory of inelastic multislice simulations

First consider the scattering path length s for plasmon excitation. The length s follows a Poisson distribution where the probability of scatter between s and $(s+ds)$ is given by $\exp(-s/\lambda_p)ds/\lambda_p$, with λ_p being the plasmon mean free path. Denote by RND a random number that is uniformly distributed over the range [0,1]. Furthermore, define RND as [20]:

$$\mathrm{RND} = \frac{\int_0^s \frac{1}{\lambda_p} \exp\left(-\frac{s}{\lambda_p}\right) ds}{\int_0^\infty \frac{1}{\lambda_p} \exp\left(-\frac{s}{\lambda_p}\right) ds} \quad \ldots (1)$$

Simplifying we obtain:

$$s = -\lambda_p \ln[1 - \mathrm{RND}] = -\lambda_p \ln(\mathrm{RND1}) \quad \ldots (2)$$

Using a computer generated, uniform random variable RND1 a series of values for the scattering length s can be obtained that are Poisson distributed about the mean value λ_p. A similar procedure can be used to estimate the scattering angle θ (see Figure 1a). By assuming the transition matrix element for a plasmon can be described by a harmonic oscillator Ferrell [21] obtained a $(\theta^2 + \theta_E^2)^{-1}$ Lorentzian distribution for the differential scattering cross-section $d\sigma/d\Omega$, where θ_E is the characteristic scattering angle given by $E_p/(2E_o)$, with E_p being the plasmon energy and E_o the incident energy of the primary electrons. Define a uniform random variable RND2 such that:

$$\mathrm{RND2} = \frac{\int_0^\theta \frac{d\Omega}{\theta^2 + \theta_E^2}}{\int_0^{\theta_c} \frac{d\Omega}{\theta^2 + \theta_E^2}} \quad \ldots (3)$$

The upper limit of θ_c for the lower integral is the maximum scattering angle for plasmon excitation, i.e. above θ_c single electron excitations are dominant [19]. Since θ_E for plasmon scattering is small, the solid angle $d\Omega = (2\pi \sin\theta) d\theta \approx (2\pi\theta) d\theta$. With this approximation Equation (3) can be simplified as:

$$\theta^2 = (\theta_c^2 + \theta_E^2)^{\mathrm{RND2}} - \theta_E^2 \quad \ldots (4)$$

Plasmon scattering is independent of the azimuthal angle ϕ (Figure 1a), which can therefore be estimated using a third uniform random variable RND3 as:

$$\phi = 2\pi(\mathrm{RND3}) \quad \ldots (5)$$

The above procedure for estimating s, θ and ϕ can be repeated to analyse multiple plasmon scattering, with the only restriction being that the sum of path lengths s must be less than the specimen foil thickness. The polar and azimuthal scattering angles in Equations (4) and (5) are however defined with respect to the electron beam direction prior to the scattering event. It is therefore convenient to choose a frame of reference such that the electron wavevector is along the z-axis (for normal beam incidence this means that the z-axis is parallel to the optic

axis). Scattering changes the orientation of the frame of reference. The electron wavevector $\mathbf{k}'$ in the scattered coordinate frame $x'y'z'$ can be expressed in the xyz frame prior to scattering via the inverse Euler rotation matrices [25]:

$$\mathbf{k} = R_{\phi}^{-1} R_{\theta}^{-1} \mathbf{k}' \quad \ldots (6a)$$

$$R_{\theta}^{-1} = \begin{pmatrix} \cos\theta & 0 & \sin\theta \\ 0 & 1 & 0 \\ -\sin\theta & 0 & \cos\theta \end{pmatrix} \quad \ldots (6b)$$

$$R_{\phi}^{-1} = \begin{pmatrix} \cos\phi & -\sin\phi & 0 \\ \sin\phi & \cos\phi & 0 \\ 0 & 0 & 1 \end{pmatrix} \quad \ldots (6c)$$

where $\mathbf{k}' = (0,0,k)$ with k being the wave number of the incident electron after correcting for energy loss (for plasmons this energy correction can be neglected). $\mathbf{k}$ is the wavevector $\mathbf{k}'$ expressed in the xyz coordinate frame. Equation (6) is used to keep track of the wavevector during multiple plasmon scattering.

In a multislice simulation the transmission function models the phase shift of the incident electrons due to the electrostatic potential of the specimen projected along the beam direction [7]. For a free electron metal the plasmon lifetime τ can be estimated from the full width at half maximum ΔE of the plasmon peak using the relation $\Delta E = h/\tau$, where h is Planck's constant [19]. From the experimental EELS results for silicon reported in this paper the lifetime τ is found to be of the order of 10^{-15} s. Furthermore, from the plasmon peak energy the oscillation period in silicon is of the order of 10^{-16} s, which is a similar time scale for a 200 kV electron to traverse a 100 nm thick specimen. Thus with plasmon excitation the valence electrons are continuously oscillating throughout the time it takes the electron beam to exit the specimen. Strictly speaking the electrostatic potential, and by extension the transmission function, should therefore be dynamically evolving. However, it can be shown that any perturbation of the electrostatic potential must be negligible for plasmon excitations. This follows from the fact that at the plasmon frequency ω_p the dielectric function $\varepsilon(\omega_p) = 0$ for an undamped system [19]. Since the electric displacement field $\mathbf{D}(\omega_p) = \varepsilon_0\varepsilon(\omega_p)\mathbf{E}(\omega_p) = \varepsilon_0\mathbf{E}(\omega_p) + \mathbf{P}(\omega_p) = 0$, at the plasma frequency the polarisation $\mathbf{P}$ must cancel the electric field $\mathbf{E}$ of the incident electron [26]. The polarisation magnitude P for valence electrons in silicon displaced by distance δ from the equilibrium positions is given by:

$$P = \frac{32\delta q}{a_o^3} \quad \ldots (7)$$

where q is the electron charge and a_o is the lattice parameter of silicon. The numerical factor of 32 in Equation (7) is due to silicon containing 8 atoms in a unit cell with 4 valence electrons per atom. Taking δ as 0.01 Å, which is approximately 1% of the (projected) 1.4 Å [110]-Si dumbbell bond, a value of 0.03 C/m^2 is obtained for P. This corresponds to an extremely large electric field of 3.6 x 10^9 V/m. The maximum electric field for the incident

electron at an impact parameter b is by Coulomb's Law $q/(4\pi\varepsilon_0 b^2)$ [27], where ε_0 is the permittivity of free space. The desired polarisation is therefore generated at an impact parameter of only 6 Å, i.e. slightly larger than the silicon unit cell dimension. Low energy excitations such as plasmons are however expected to be delocalised over distances much larger than the lattice periodicity [28], so that the valence electron displacement δ should in reality be much smaller than the 0.01 Å value assumed here. Furthermore, the electrostatic potential is determined by all atomic electrons and nuclei, and not just the valence electrons undergoing plasmon oscillations. This suggests that the electrostatic potential can be assumed to be constant during plasmon excitation. However, for the transmission function the key parameter is the potential projected along the beam direction [22], and hence the tilt of the electron beam following plasmon scattering must be taken into account. This is done using the procedure outlined below.

Using Kirkland's atom scattering factors [7] the projected potential $V_p(\mathbf{R})$ is expressed as:

$$V_p(\mathbf{R}) = \frac{\pi a_B q}{\varepsilon_0}\sum_i a_i\, K_0\left(2\pi R\sqrt{b_i}\right) + \frac{\pi a_B q}{2\varepsilon_0}\sum_i \frac{c_i}{d_i}\exp\left(-\frac{\pi^2 R^2}{d_i}\right) \quad \ldots (8)$$

where a_B is the Bohr radius and K_0 is the modified Bessel function of the second kind. a_i,b_i and c_i,d_i are respectively constants in the Lorentzian and Gaussian expansion terms of the atom scattering factor [7]. The two-dimensional position vector $\mathbf{R}$ is defined in the plane of the specimen perpendicular to the optic z-axis. The geometry for a tilted beam is illustrated schematically in Figure 1b. For a spherically symmetric atom the projected potential $V_p'(\mathbf{R})$ along the tilted beam direction only depends on the perpendicular distance $|\boldsymbol{r}'|$ from the origin to the incident ray at $\mathbf{R}$ (Figure 1b). If (x',y',z') are the position coordinates of $\boldsymbol{r}'$ it can be shown that (see Appendix):

$$z' = -\frac{1}{2}(x\cos\phi + y\sin\phi)\sin(2\alpha) \quad \ldots (9a)$$

$$x' = x + \left(\frac{z'}{\tan\alpha}\right)\cos\phi \quad \ldots (9b)$$

$$y' = y + \left(\frac{z'}{\tan\alpha}\right)\sin\phi \quad \ldots (9c)$$

where $\mathbf{R} = (x,y)$ and $\alpha = [(\pi/2) - \theta]$. $r' = [(x')^2 + (y')^2 + (z')^2]^{½}$ is then substituted for R in Equation (8) to obtain $V_p'(\mathbf{R})$. Following Ishizuka [22] the transmission function $\mathbf{Q}(\mathbf{R})$ for tilted illumination is given by:

$$\mathbf{Q}(\mathbf{R}) = \exp\left[i\sigma\left(\frac{k}{k_z}\right)V_p'(\mathbf{R})\right] \quad \ldots (10)$$

where σ is the interaction constant, k is the wave number and k_z the wavevector component along the optic z-axis. The small change in σ and k due to plasmon excitation can be ignored, although this would not be the case for larger energy losses. The use of a modified projected potential $V_p'(\mathbf{R})$ in the transmission function (Equation 10) means that the phase shift due to inelastic plasmon scattering is accounted for. Compare this with the frozen phonon approach where, due to limitations of the model, the TDS scattered wave is always coherent with the elastic wave. The reciprocal space propagator function $\mathbf{P}(\mathbf{u})$ for tilted illumination is given by [22]:

$$\mathbf{P}(\mathbf{u}) = \left(\frac{k_z}{k}\right)\exp(2\pi i s_u \Delta z) \quad \ldots (11a)$$

$$s_u = \frac{(k^2 - k_z^2) - (k_x + u_x)^2 - \left(k_y + u_y\right)^2}{2k_z} \quad \ldots (11b)$$

where $\mathbf{u} = (u_x, u_y)$ is the two-dimensional reciprocal vector and s_u is its deviation parameter. k_x, k_y are wavevector components along the x- and y-axes respectively and Δz is the slice thickness. k_x, k_y and k_z following plasmon scattering are determined from Equations 6a-6c.

When implementing the inelastic multislice algorithm the simulation initially assumes normal beam incidence and elastic scattering until the plasmon scattering depth is reached. The scattering depth is determined by Equation (2). At this stage the transmission and propagator functions must be modified to Equations (10) and (11) respectively, with the plasmon scattering angles determined by Equations (4) and (5). The modified transmission and propagator functions are used to propagate the plasmon scattered electron beam until it exits the specimen or in the case of multiple scattering to the next plasmon scattering depth, whence the transmission and propagator functions are updated. Frozen phonons can also be included to model TDS. Several supercells can be constructed to simulate alternative scenarios of no plasmon scattering (i.e. phonon only or zero energy loss), single plasmon scattering, double plasmon scattering and so on. For example, each supercell for single plasmon scattering will have a unique frozen phonon configuration and unique plasmon scattering depth and scattering angle. The simulated results from each group (e.g. single plasmon scattering) are then incoherently summed to give a statistical average. For a specimen of thickness t the fraction of incident electrons undergoing N plasmon scattering events is governed by Poisson statistics [19]. Therefore in order to obtain the energy unfiltered result (e.g. HAADF signal etc.) a suitable weighting must be applied to the statistically averaged result from each group before adding them together. For N plasmon scattering events the relative weighting (w_N) is given by [19]:

$$w_N = \frac{1}{N!}\left(\frac{t}{\lambda_p}\right)^N \exp\left(-\frac{t}{\lambda_p}\right) \quad \ldots (12)$$

The weighting in Equation (12) assumes that all multiple scattering events are simulated, while in practice it is only possible to simulate up to a finite value of N. The value of N will depend on the specimen thickness, with thicker samples requiring larger N compared to thinner samples. Hence care must be taken when comparing simulation results which have different values of N or results for the same N but different specimen thicknesses.

Inelastic multislice simulations assume that plasmon scattering has a Lorentzian angular distribution, which is valid when the incident electron is a plane wave and when the scattered wavevector lies on an Ewald sphere [21]. However, in a crystal the incident electrons are Bloch waves and scattering is along hyperbolic shaped dispersion surfaces [28]. Nevertheless Howie [28] has shown that, at least for the two-beam case, these corrections are negligible for small angle plasmon scattering. This is perhaps not surprising since plasmon excitation is highly delocalised and therefore should not be sensitive to the rapid fluctuations in crystal potential. Furthermore, for long range interactions inelastic scattering predominantly takes place via intraband Bloch wave transitions [28]. Since interband transitions are suppressed the scattering cross-section should largely be independent of depth. For example, although the strongly channeling 1s states may be depleted at large specimen thickness plasmon scattering can still take place via the weakly channeling non-1s states. This means that the plasmon mean free path λ_p can be assumed to be constant and independent of specimen thickness. The delocalised nature of the plasmon excitation is therefore crucial for the physical validity of the inelastic multislice method.

3. Experimental and simulation methods

The inelastic multislice simulation method is applied to convergent beam electron diffraction (CBED) patterns of [110]-Si. The silicon sample was prepared using argon ion-beam milling. Energy filtered CBED patterns were acquired at 200 kV in a JEOL 2100F FEG TEM with Gatan Tridiem electron energy loss spectroscopy (EELS) spectrometer. The probe semi-convergence angle was 3.9 mrad and the spectrometer collection semi-angle was 20 mrad. Energy filtered CBED patterns were acquired at 0 eV (i.e. zero loss peak filtered), 17 eV (single plasmon), 33 eV (double plasmon) and 50 eV (triple plasmon) with 10 eV energy window. Relatively thick regions of the sample were deliberately selected in order to have a strong enough signal for multiple plasmon scattering. (t/λ) for the three different regions analysed were 1.5, 2.3 and 3.3 respectively and corresponds to a specimen thickness of ~162 nm, 254 nm and 362 nm respectively [29]. When estimating (t/λ) the spectrometer dispersion was adjusted to increase the energy loss range as much as possible without saturating the zero loss peak; for the two thinnest specimens the maximum energy loss was 185 eV, while for the thickest specimen the maximum energy loss was 370 eV.

Kirkland's atom scattering factors [7] were used in the inelastic multislice simulations. Frozen phonon configurations were generated assuming a 0.078 Å rms displacement for silicon [7] and Einstein approximation of uncorrelated harmonic oscillators [5]. The plasmon mean free path was estimated to be 105 nm (section 4.1). The critical plasmon scattering angle θ_c for silicon was 27.6 mrad [30]. CBED simulations were carried out for a 160 nm thick, [110]-Si supercell with lateral dimensions of 53.8 Å x 54.3 Å. The projected potential was sampled using a 1024 x 1024 pixel array and the slice thickness was 1.9 Å (i.e. atomic

layer spacing along [110]). The probe parameters were 200 kV accelerating voltage, 3.9 mrad semi-convergence angle, 1 mm spherical aberration coefficient and -60 nm Scherzer underfocus. 'Zero loss', single, double and triple plasmon scattering were simulated with 50 supercell configurations for each scattering mechanism (for convenience the term 'zero loss' is used even in the presence of phonon scattering). Although 50 configurations were simulated for better statistics in practice a good degree of convergence was apparent even for 10 configurations. The same 50 frozen phonon configurations were used for all scattering mechanisms. The normalised intensity of the exit wavefunction was always above 0.9 for 'zero loss' scattering, while for single, double and triple plasmon scattering this was true for 88%, 80% and 72% of the cases respectively.

The HAADF intensity across the [110]-Si dumbbells was also calculated for 10 nm and 50 nm thick specimens. The probe parameters were 200 kV accelerating voltage, 20 mrad semi-convergence angle and zero electron optic aberrations. The HAADF detector inner angle was 80 mrad. The supercell had lateral dimensions of 26.9 Å x 27.1 Å and the projected potential was sampled using a 512 x 512 pixel array with a slice thickness of 3.8 Å (i.e. periodic repeat distance along [110]). 'Zero loss' and single plasmon scattering were simulated for the 10 nm sample, while double plasmon scattering was also included for the 50 nm sample. 50 supercell configurations were simulated for each scattering mechanism, with the frozen phonon configurations being re-used to reduce computation time.

4. Results and Discussion

4.1. *Experimental results*

Figure 2a shows the EELS spectrum for the ~362 nm thick region of [110]-Si sample. At least five plasmon peaks are visible. Since the plasmon peak intensities follow a Poisson distribution [19] a graph of $\ln(N!I_N/I_0)$ vs N should be a straight line with gradient $\ln(t/\lambda_p)$, where N is the number of plasmon multiple scattering events (e.g. single, double scattering etc). The intensity I_N of the multiple plasmon scattered peak was determined by least squares fitting a Gaussian. The $\ln(N!I_N/I_0)$ vs N plot is shown in Figure 2b and from the least squares fitted straight line a value of 3.16 is obtained for (t/λ_p). The log-ratio method [19] gave a (t/λ) relative thickness of 3.29. Using these two values and the fact that the inelastic mean free path λ is estimated to be 110 nm [29] gives a λ_p value of ~105 nm, which was used in the inelastic multislice simulations as described in section 3.

Figure 3 shows the first few zero order Laue zone (ZOLZ) reflections in [110]-Si CBED patterns acquired at different specimen thicknesses of 162, 254 and 362 nm. At each specimen thickness energy filtering was used to acquire the 'zero loss', single plasmon (17 eV), double plasmon (33 eV) and triple plasmon (50 eV) scattered CBED patterns. At each specimen thickness the relative intensity of the unscattered disc with respect to Bragg diffracted discs, as well as the contrast of the rocking beam pattern within individual discs, diminish with increasing energy loss. The 'blurring' of the rocking beam pattern is less pronounced for the unscattered beam compared to Bragg diffracted beams. Interestingly the rocking beam pattern is still discernible in the thickest region of the specimen even after multiple plasmon scattering. This is likely due to the fact that plasmon excitation largely

takes place through intraband Bloch wave transitions [28], so that at large specimen thicknesses, where the 1s Bloch state should be depleted, inelastic scattering can still take place via the non-1s Bloch states, which are more strongly transmitted.

In Figure 4 a larger section of the CBED pattern is plotted on a logarithmic intensity scale to reveal excess Kikuchi bands and Kikuchi lines. As with the rocking beam patterns for a given specimen thickness the contrast of the Kikuchi bands and lines diminish with increasing energy loss. This is illustrated in Figure 5 which plots the intensity profile of the $002/00\bar{2}$ Kikuchi band. The intensity was integrated over the box region in Figure 4a. For visual clarity only the intensity profiles for the two extreme cases of 'zero loss' and triple plasmon loss are shown, with the intensity within the Kikuchi band normalised for direct comparison. The intensity dip at the edges of the Kikuchi band are less pronounced for the triple plasmon loss, which results in lower contrast. The mechanism for excess Kikuchi band formation is described in [31]. Both the incident and scattered high energy electrons form Bloch waves within the crystal. Excess Kikuchi bands are due to high angle TDS scattering from Bloch waves with peak intensity at the atom column positions, such as the 1s state. By the principle of reciprocity the direction of scattering can be reversed, from which it follows that the TDS scattered Bloch wave must also be strongly channeling. Systematic row Bloch wave calculations indicate that for incident wavevectors within the Kikuchi band (i.e. negative deviation parameter) the 1s Bloch state is preferentially excited [31], which is the condition for excess Kikuchi band intensity. Plasmon scattering will however change the direction of the incident wavevector within the specimen. The rocking beam patterns for the transmitted and diffracted beams must therefore be convolved with the spread in illumination angles due to plasmon excitation, which effectively reduces the contrast of the Kikuchi bands, as seen in Figure 5.

4.2. *Simulation results*

In inelastic multislice simulations plasmon scattering depths are randomly generated from a Poisson distribution with mean free path λ_p. Figure 6a shows cumulative distribution plots for the depth at which the first scattering event takes place for single, double and triple plasmon scattering in a 160 nm thick silicon specimen (this thickness corresponds to the thinnest region analysed in section 4.1). Values from the 50 supercell configurations simulated were used for generating the plot. For multiple plasmon scattering all scattering events must take place before the incident electron exits the specimen; hence for a given specimen thickness the first scattering event occurs (on average) closer to the specimen entrance surface as the number of scattering events increase. This is evident from Figure 6a. From section 2 the main effect of plasmon excitation is a tilting of the electron beam due to the scattering angle, rather than the small energy loss. For silicon the characteristic plasmon scattering angle θ_E is 0.04 mrad at 200 kV. If plasmon scattering took place at the specimen entrance surface then for a 160 nm foil the lateral deviation of the electron beam at the exit surface is 0.07 Å. This is a similar magnitude to the rms displacement of silicon atoms due to thermal vibrations, and in this case suggests that the projected potential of an atom column, as 'seen' by the electron beam, is similar between plasmon and TDS scattering mechanisms. Therefore plasmon excitation can have a non-negligible effect on electron beam scattering, particularly if the scattering takes place close to the specimen entrance surface, such as, for example, during

multiple scattering. Figure 6b is a histogram for the plasmon scattering angles obtained from the 50 supercell configurations used for simulating single plasmon scattering. The majority (>50%) of scattering events occur at angles <2 mrad due to the small value of θ_E, although scattering to much larger angles that approach θ_c (27.6 mrad) is also possible, though less likely. Dynamic diffraction within the specimen will be significantly perturbed for these large angle scattering events.

Figure 7 shows the simulated [110]-Si CBED patterns for a 160 nm thick foil at 'zero loss' as well as single, double and triple plasmon losses respectively. The contrast of the rocking beam patterns in the central ZOLZ region (Figures 7a-7d) decrease monotonically with energy loss, with the decrease being more prominent within the Bragg discs compared to the unscattered beam. The relative intensity of the unscattered beam with respect to the diffracted beams also decreases with energy loss. Plotting the CBED intensity on a logarithmic scale reveals the Kikuchi bands and lines (Figures 7e-7h). Multiple plasmon excitation is found to monotonically decrease the contrast of these features. This is demonstrated in Figure 8 which plots the intensity profiles of the $002/00\bar{2}$ Kikuchi bands for 'zero loss' and triple plasmon loss CBED patterns. The intensity profiles were extracted from the box region shown in Figure 7e; the region is approximately the same as that used for the experimental CBED patterns (Figure 4a). Furthermore, the intensity within the Kikuchi bands were normalised for a direct visual comparison. The intensity dip at the Kikuchi band edges is less pronounced for triple plasmon energy loss. The agreement between experimental and simulated Kikuchi band intensities in Figures 5 and 8 is good, both in terms of the profile shape and normalised intensity values. This observation, along with the fact that other important features of the CBED pattern (e.g. rocking curves, relative intensities etc) are also reproduced, suggests that the inelastic multislice method can accurately simulate plasmon excitations within the material. Note that the simulated results also show a higher order Laue zone (HOLZ) ring for all energy losses (Figures 7e-7h), but unfortunately the camera length for the experimental diffraction patterns in Figure 4 was too large to capture this.

HAADF intensity profiles across [110]-Si dumbbells have also been simulated in 10 and 50 nm thick specimens to examine the role of plasmon scattering on resolution and atom column contrast. From Poisson statistics [19] the single plasmon intensity is ~10% of the 'zero loss' intensity in a 10 nm thick silicon specimen. This value increases to 48% for a 50 nm thick specimen, while the double plasmon intensity is 11% of the 'zero loss' intensity. Therefore even for relatively thin specimens a significant fraction of the HAADF intensity is due to plasmon loss electrons. Figure 9a shows the HAADF profiles for 'zero loss' and single plasmon scattered electrons in the 10 nm thick specimen. The HAADF intensity displayed in the figure is the integrated value for the 50 supercell configurations simulated; the weighting w_N (Equation 12) has not been applied. The supercells contain frozen phonons, so that TDS is also included in the simulations. Although the absolute value of the HAADF intensity decreases due to plasmon scattering the peak-to-background ratio is relatively constant at 26.4 ± 1.6 for 'zero loss' and 28.7 ± 1.7 for single plasmon loss (the error is based on the peak-to-background ratio values for the two atom columns). Furthermore, the atom column resolution is unchanged by plasmon scattering. These trends are also observed for the 50 nm thick specimen (Figure 9b). The peak-to-background ratios are 10.2 ± 0.1, 10.5 (<0.1 error) and 11.1 ± 0.1 for the 'zero loss', single plasmon and double plasmon profiles. The main

effect of plasmon scattering therefore appears to be a decrease in the absolute intensity per scattered electron, rather than a loss of resolution or atom column contrast. The inclusion of frozen phonons in a conventional multislice simulation also decreases the absolute HAADF intensity, compared to the equilibrium static atom case [32]. This is because thermal displacement of individual atoms 'smears' out the projected potential, causing weaker channeling of the electron beam along atom columns. The plasmon scattering angle is likely to play a similar role in reducing channeling, thereby suppressing high-angle scattering towards the HAADF detector. The decrease in absolute HAADF intensity per scattered electron could be important for quantitative atom counting techniques [3,33], especially when there is a large difference in the number of atoms between different columns, since plasmon scattering increases monotonically with specimen thickness.

5. Summary and Outlook

The inelastic multislice simulations in this paper include plasmon excitation, the dominant energy loss mechanism for high energy incident electrons. It is shown that plasmons have negligible effect on the specimen electrostatic potential; the largest changes are due to a tilting of the incident beam due to the plasmon scattering angle. The transmission and propagator functions in the multislice algorithm are modified accordingly, with the scattering angle and depth estimated using a random number based Monte Carlo approach. By combining with frozen phonons elastic, TDS and plasmon scattering can be simulated simultaneously. Simulations reproduce the many features observed in experimental [110]-Si CBED patterns, such as lower rocking beam and Kikuchi band contrast with multiple plasmon energy loss. Further simulations of the [110]-Si dumbbell HAADF intensity profile suggest that resolution and peak-to-background ratio of the atom columns are not significantly affected by plasmon excitation, although the absolute HAADF intensity per scattered electron decreases. Conventional frozen phonon multislice simulations would therefore overestimate the increase in HAADF signal with specimen thickness, so that plasmon losses must be taken into account for a full quantitative analysis.

It is of interest to consider if core electron ionisation losses could also be simulated, along with plasmons, using a similar procedure. Although the ionisation cross-section is much smaller than plasmon excitation it is the signal of interest in (say) X-ray mapping, which can be carried out at atomic resolution using large solid angle detectors. Significant errors in composition analysis are nevertheless present if dynamic diffraction of the incident electrons are not taken into account [34], and hence the need for robust simulation methods. The specimen electrostatic potential is strongly perturbed by core electron ionisation. The potential of the ionised atom in the transmission function (Equation 10) has to be replaced by one that contains a (partially screened) core hole, in order to model the phase shift due to inelastic scattering. The scattering angle has a Lorentzian distribution [19], so that the tilt of the incident beam can be estimated using the same procedure developed here for plasmons. However, the assumed scattering cross-section, which determines both the angular distribution and mean free path, is only valid for an incident plane wave, while in a crystal the high energy electrons form Bloch waves, so that the scattering cross-section includes an additional mixed dynamic form factor term [35]. Without this modification the simulations cannot reproduce the strong channeling dependence of the X-ray signal [36-37]. In fact

delocalisation of the inelastic scattering is essential for application of Monte Carlo based techniques in multislice. It is therefore expected to work well for plasmons and interband transitions, but not for high energy core loss ionisation of atoms in a crystal.

Acknowledgements

BGM would like to thank the late Mr Brian Miller (University of Glasgow) for preparing the silicon sample.

Appendix

In this section Equations (9a)-(9c) will be derived. With reference to Figure 1b consider an arbitrary point (x'',y'',z'') along the straight line *AB*, which represents a tilted electron beam 'ray'. The projected length l of (x'',y'',z'') in the equatorial plane is ($z''/\tan\alpha$). By geometry the following relations are obtained:

$$x'' = x + \left(\frac{z''}{\tan\alpha}\right)\cos\phi \quad \ldots \text{(A1)}$$

$$y'' = y + \left(\frac{z''}{\tan\alpha}\right)\sin\phi \quad \ldots \text{(A2)}$$

Equations (A1) and (A2) are analytical solutions that are valid for any point along *AB*. Define $\boldsymbol{r}' = (x',y',z')$ as the perpendicular vector from the origin *O* to the straight line *AB*. From Figure 1b:

$$\boldsymbol{r}' = x'\mathbf{i} + y'\mathbf{j} + z'\mathbf{k} \quad \ldots \text{(A3)}$$

$$\mathbf{t} = (x - x')\mathbf{i} + (y - y')\mathbf{j} - z'\mathbf{k} \quad \ldots \text{(A4)}$$

where **i**, **j**, **k** are the unit basis vectors. $\boldsymbol{r}'\cdot\mathbf{t} = 0$ then leads to Equation (9a). In obtaining this result Equations (A1) and (A2), as applied to (x',y',z'), have been substituted for x' and y' in Equations (A3) and (A4). This is valid since $\boldsymbol{r}'$ lies on the straight line *AB*. Equations (9b) and (9c) are essentially Equations (A1) and (A2) as applied to (x',y',z').

References

[1] P.B. Hirsch, A. Howie, R.B. Nicholson, D.W. Pashley, M.J. Whelan, *Electron Microscopy of Thin Crystals*, Butterworths, 1965.
[2] D.O. Klenov, S. Stemmer, *Ultramicroscopy* **106** (2006) 889.
[3] J.M. LeBeau, S.D. Findlay, L.J. Allen, S. Stemmer, *Nano Lett.* **10** (2010) 4405.
[4] C.R. Hall, P.B. Hirsch, *Proc. Roy. Soc. A* **286** (1965) 158.
[5] R.F. Loane, P. Xu, J. Silcox, *Acta Cryst. A* **47** (1991) 267.
[6] P. Goodman, A.F. Moodie, *Acta Cryst. A* **30** (1974) 280.

[7] E.J. Kirkland, *Advanced Computing in Electron Microscopy*, 2nd Edition, Springer, USA, 2010.
[8] B.D. Forbes, A.V. Martin, S.D. Findlay, A.J. D'Alfonso, L.J. Allen, *Phys Rev B* **82** (2010) 104103.
[9] Z.L. Wang, *Acta Cryst. A* **54** (1998) 460.
[10] D. Van Dyck, *Ultramicroscopy* **109** (2009) 677.
[11] I. Lobato, D. Van Dyck, *Ultramicroscopy* **156** (2015) 9.
[12] W. Van den Broek, X. Jiang, C.T. Koch, *Ultramicroscopy* **158** (2015) 89.
[13] D.A. Welch, R. Faller, J.E. Evans, N.D. Browning, *Ultramicroscopy* **135** (2013) 36.
[14] M.E. Holtz, Y. Yu, J. Gao, H.D. Abruna, D.A. Muller, *Microsc. Microanal.* **19** (2013) 1027.
[15] H. Yoshioka, *J. Phys. Soc. Jpn*, **12** (1957) 618.
[16] W. Coene, D. Van Dyck, *Ultramicroscopy* **33** (1990) 261.
[17] C. Dwyer, *Ultramicroscopy* **104** (2005) 141.
[18] L.J. Allen, A.J. D'Alfonso, S.D. Findlay, *Ultramicroscopy* **151** (2015) 11.
[19] R.F. Egerton, *Electron Energy-Loss Spectroscopy in the Electron Microscope*, Plenum Press, New York, 1996.
[20] D.C. Joy, *Monte Carlo Modelling for Electron Microscopy and Microanalysis*, Oxford University Press, 1995.
[21] R.A. Ferrell, *Phys. Rev.* **101** (1956) 554.
[22] K. Ishizuka, *Acta Cryst. A* **38** (1982) 773.
[23] Z.L. Wang, P. Lu, *Ultramicroscopy* **26** (1988) 217.
[24] Z.L. Wang, *Acta Cryst. A* **45** (1989) 193.
[25] J. Frank, *Three-Dimensional Electron Microscopy of Macromolecular Assemblies*, Oxford University Press, 2006.
[26] C. Kittel, *Introduction to Solid State Physics*, 8th Edition, John Wiley & Sons, 2005.
[27] J.D. Jackson, *Classical Electrodynamics*, John Wiley & Sons , 1975.
[28] A. Howie, *Proc. Roy. Soc. A* **271** (1963) 268.
[29] T. Malis, S.C. Cheng, R.F. Egerton, *J. Electron Microsc. Tech.* **8** (1988) 193.
[30] H. Raether, *Excitations of plasmons and interband transitions by electrons*. Springer Tracts in Modern Physics, vol. 88, Springer, Berlin, 1980.
[31] L. Reimer, *Transmission Electron Microscopy: Physics of Image Formation and Microanalysis*, Springer-Verlag, 1984.
[32] B.G. Mendis, *Electron Beam-Specimen Interactions and Simulation Methods in Microscopy*, Wiley, 2018.
[33] S. Van Aert, K.J. Batenburg, M.D. Rossell, R. Erni, G Van Tendeloo, *Nature* **470** (2011) 374.
[34] G. Kothleitner, M.J. Neish, N. R. Lugg, S.D. Findlay, W. Grogger, F. Hofer, L.J. Allen, *Phys. Rev. Lett.* **112** (2014) 085501.
[35] H. Kohl, H. Rose, *Adv. Electron. Electron Phys.* **65** (1985) 173.
[36] J.C.H. Spence, J. Taftø, *J. Microsc.* **130** (1983) 147.
[37] I.P. Jones, *Adv. Imaging Electron Phys.* **125** (2002) 63.

Figures

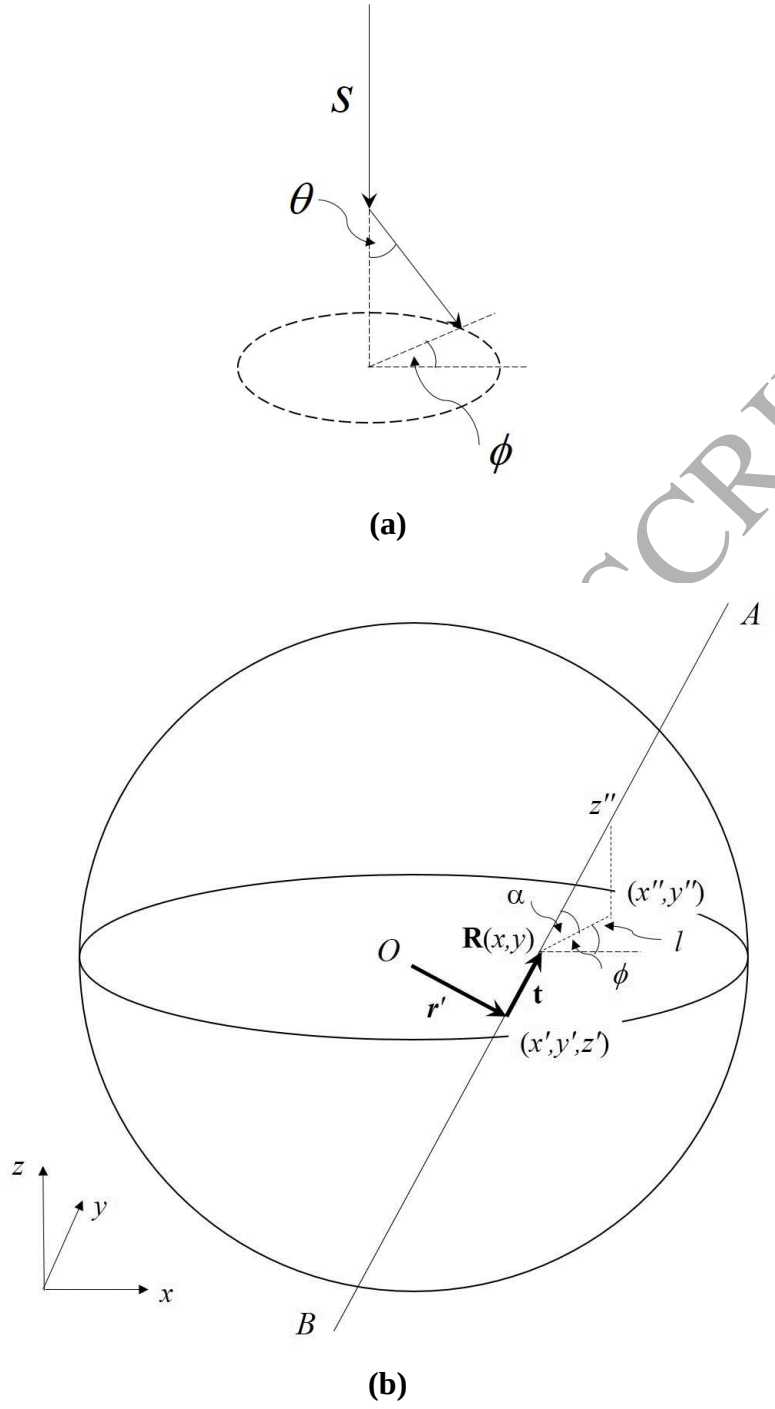

Figure 1: (a) schematic of the plasmon scattering geometry, showing the scattering path length *s*, as well as scattering polar θ and azimuthal ϕ angles. (b) is a schematic for calculating the projected atomic potential at point **R**(*x*,*y*) on the equatorial plane for a tilted beam incident along the *AB* direction. The atom is at the origin *O* and the vector **r′** is the perpendicular to the line *AB*. See text for further details.

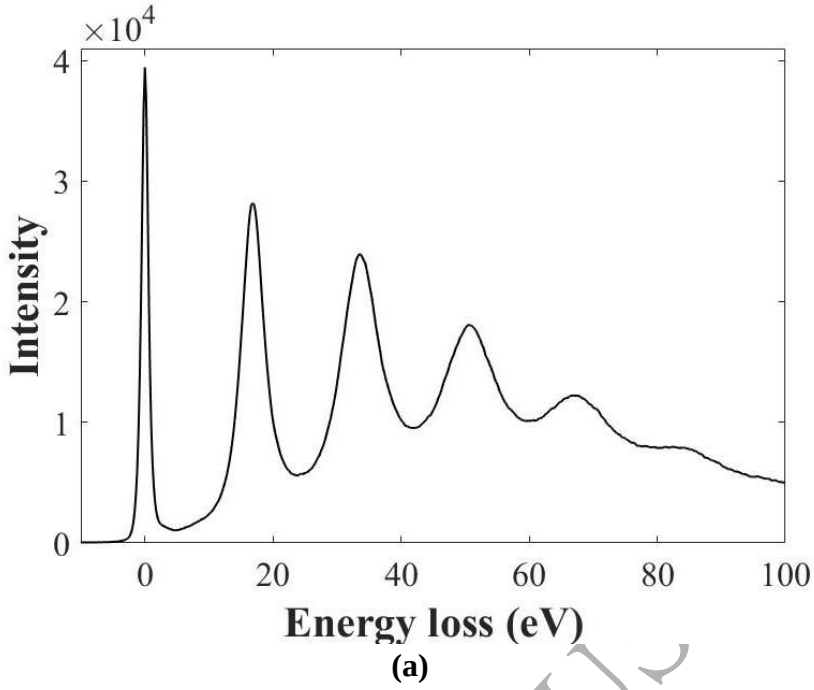

(a)

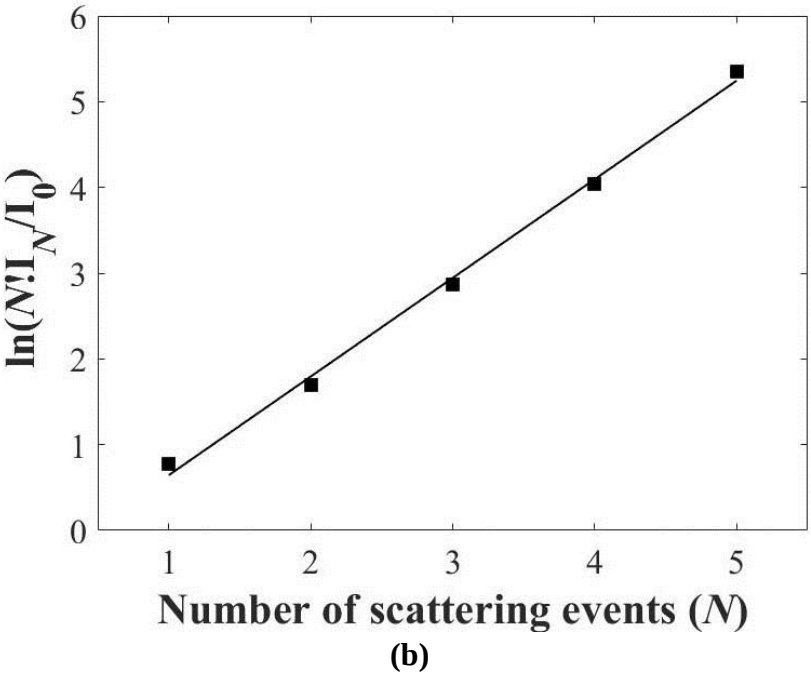

(b)

Figure 2: (a) EELS spectrum for a ~362 nm thick region of [110]-Si showing multiple plasmon peaks. (b) is the corresponding plot of $\ln(N!I_N/I_0)$ vs. N, where I_N is the intensity of the plasmon peak scattered N number of times.

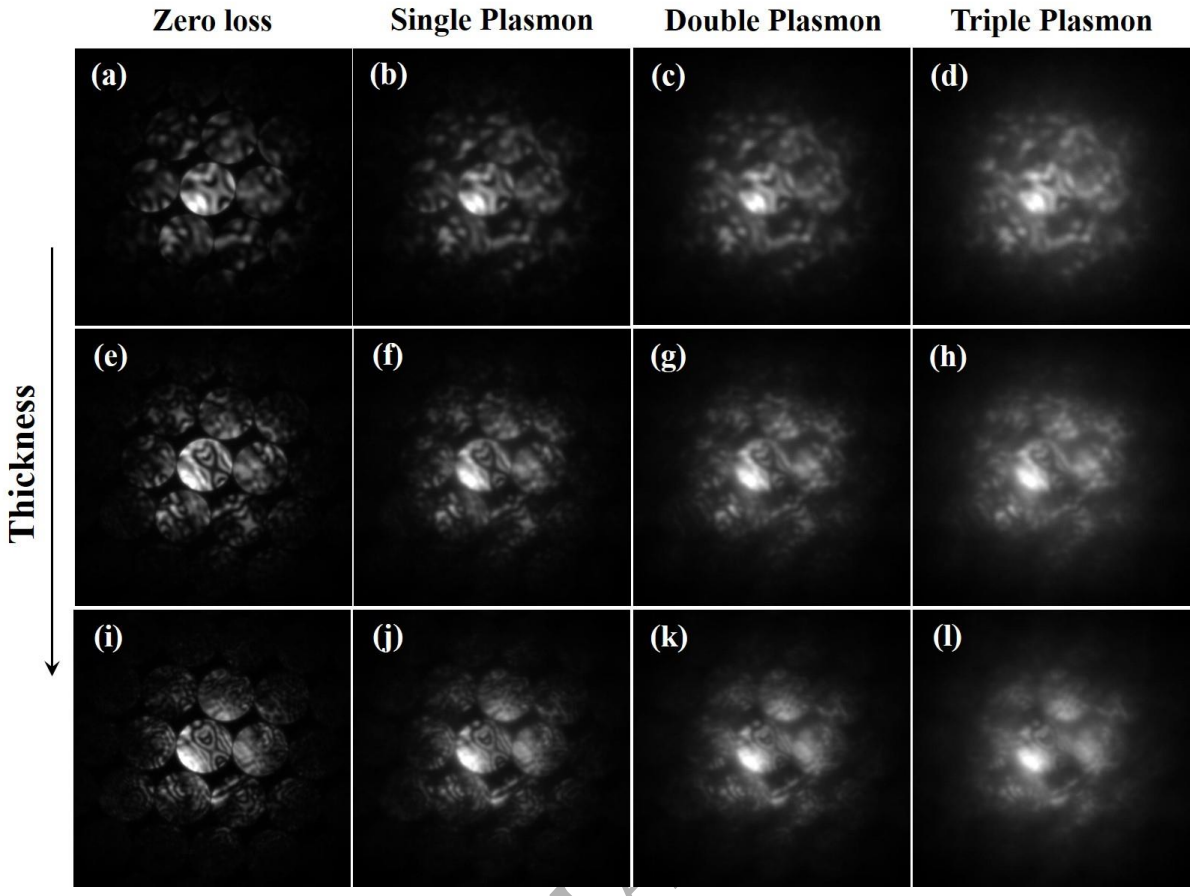

Figure 3: Central zero order Laue zone (ZOLZ) region for energy filtered, [110]-Si CBED patterns acquired at 'zero loss', as well as single, double and triple plasmon losses. The specimen thickness is 162 nm for Figures (a) to (d), 254 nm for Figures (e) to (h) and 362 nm for Figures (i) to (l) respectively. Each diffraction pattern is displayed utilising the full 4-bit image greyscale.

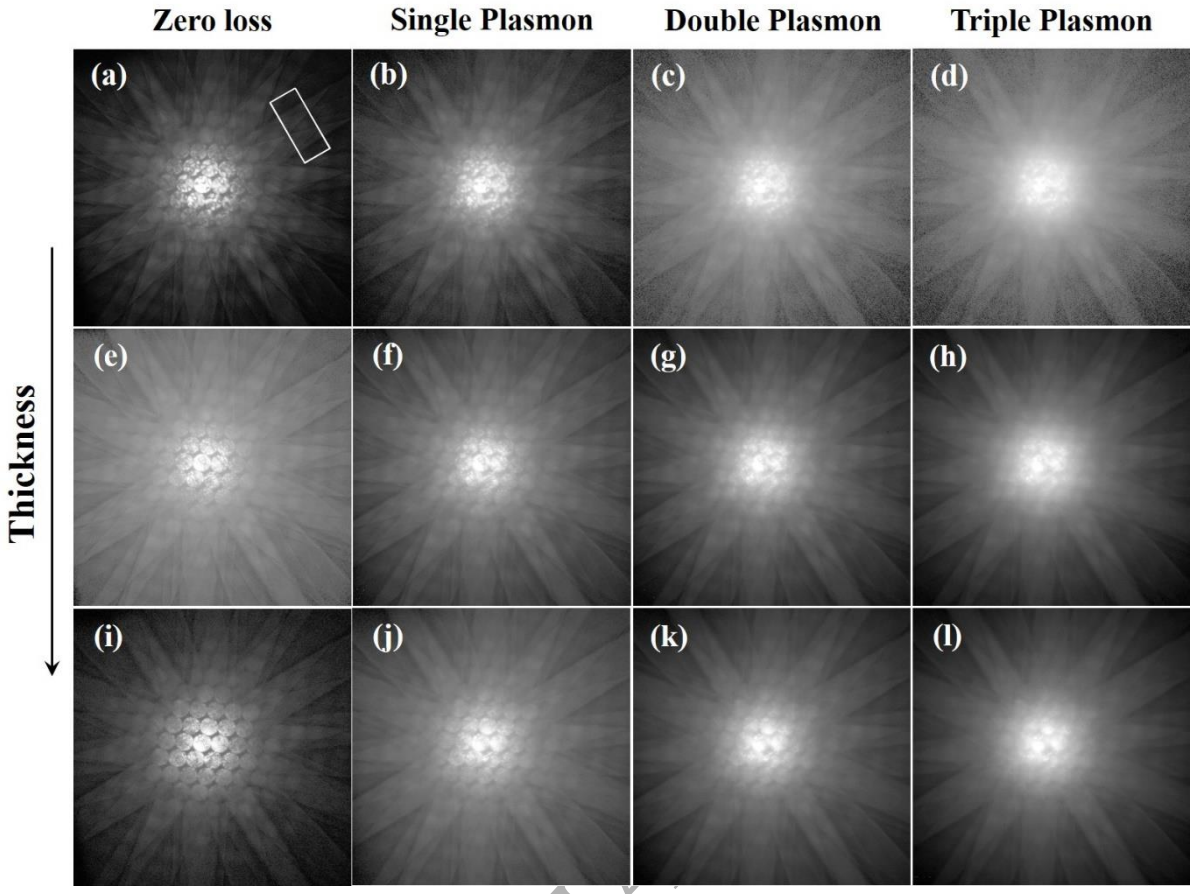

Figure 4: Energy filtered, [110]-Si CBED patterns acquired at 'zero loss', as well as single, double and triple plasmon losses, with the intensity displayed on a logarithmic scale. The specimen thickness is 162 nm for Figures (a) to (d), 254 nm for Figures (e) to (h) and 362 nm for Figures (i) to (l) respectively. Each diffraction pattern is displayed utilising the full 4-bit image greyscale.

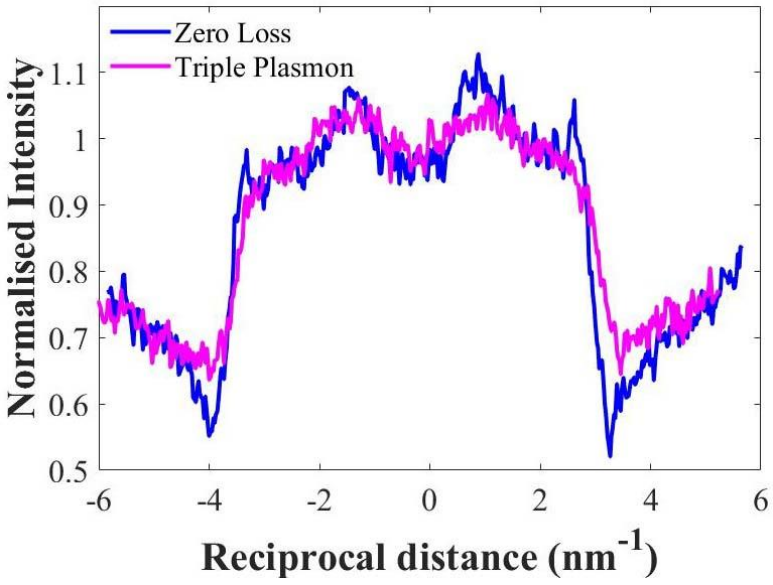

Figure 5: Intensity profiles across the $002/00\bar{2}$ Kikuchi band in 162 nm thick, [110]-Si for zero loss and triple plasmon energy loss. The intensity profile was extracted from the box region in Figure 4a. The integrated intensity within the Kikuchi band was normalised for a direct visual comparison.

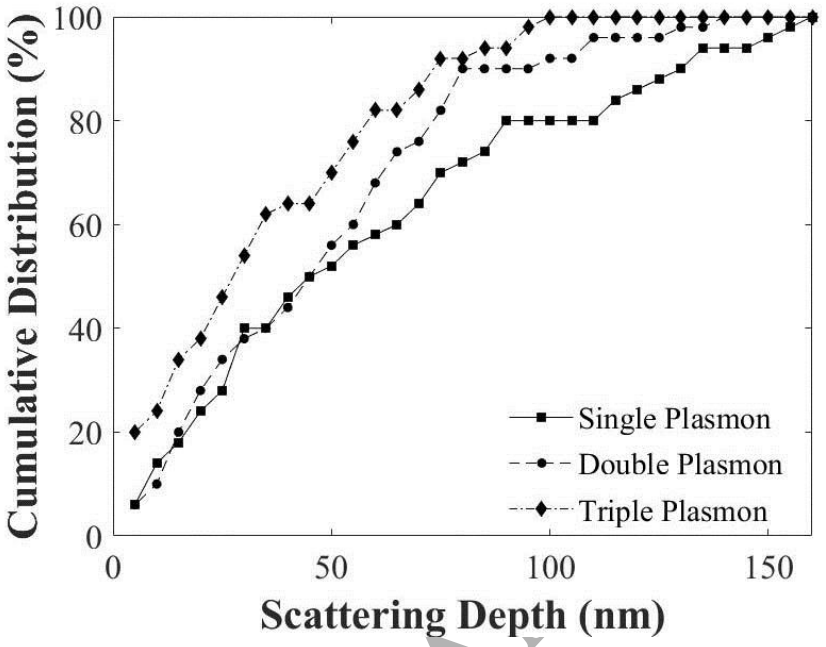

(a)

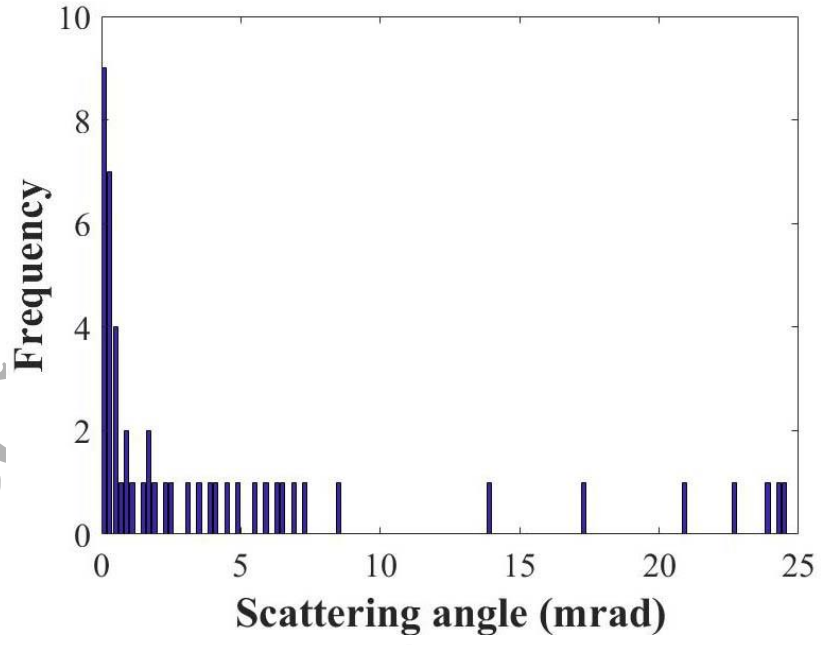

(b)

Figure 6: (a) cumulative distribution plots for the (simulated) depth of the first plasmon scattering event in a 160 nm thick silicon specimen. Curves for single, double and triple plasmon scattering are shown superimposed. (b) is a histogram of the plasmon scattering angle in silicon, constructed using data from the 50 configurations used for modelling single plasmon scattering.

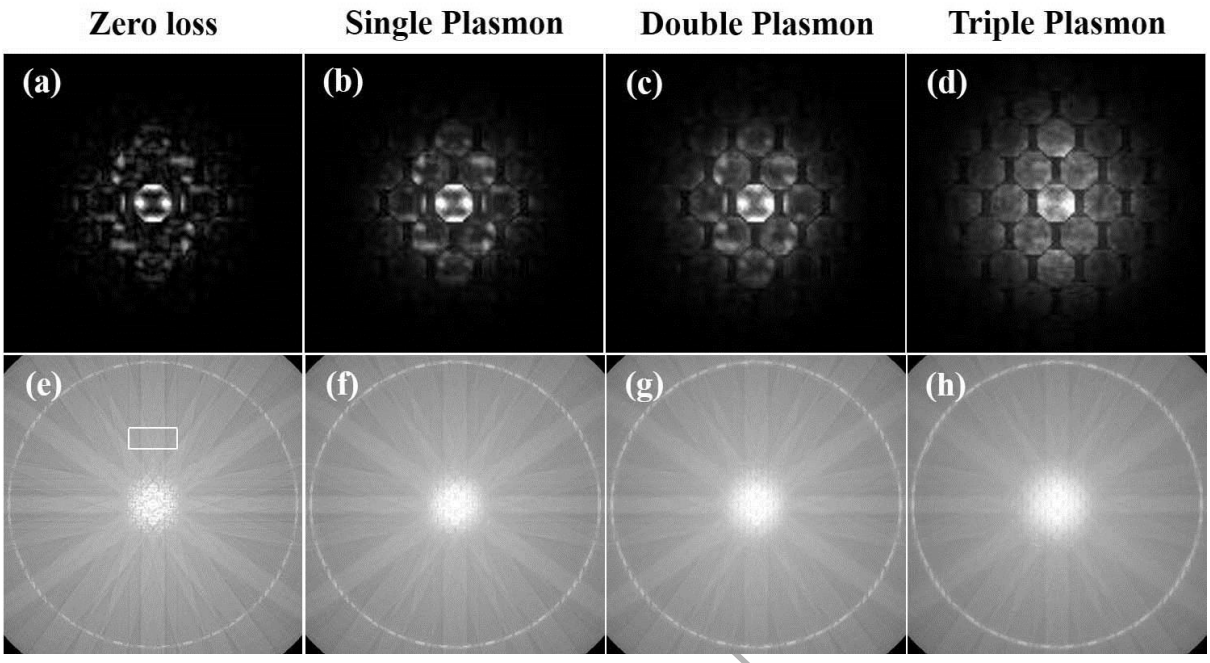

Figure 7: Simulated results for 160 nm thick, [110]-Si CBED patterns at 'zero loss', as well as single, double and triple plasmon energy losses respectively. Figures (a)-(d) show the central zero order Laue zone (ZOLZ) region, while Figures (e)-(h) are the diffraction patterns displayed on a logarithmic intensity scale. The dark regions at the corners of Figures (e)-(h) are due to bandwidth limiting in the multislice simulation. Each diffraction pattern is displayed utilising the full 4-bit image greyscale.

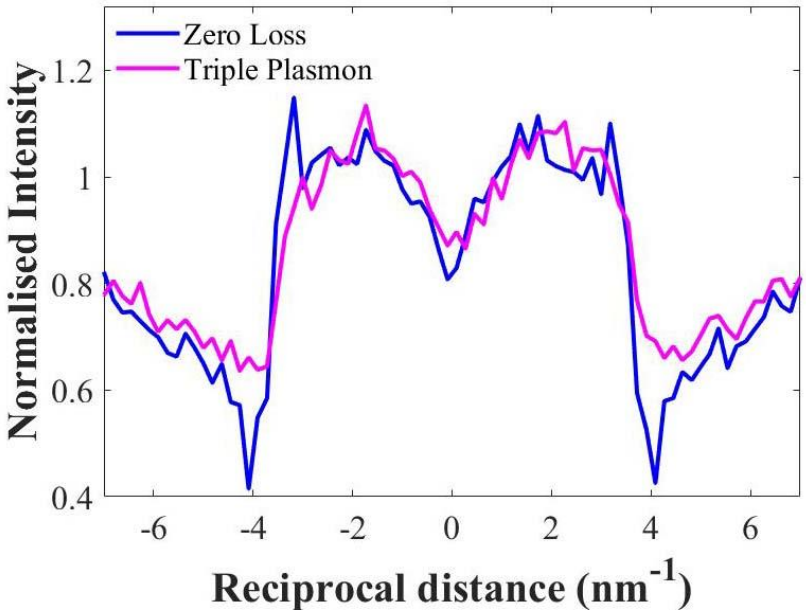

Figure 8: Intensity profiles across the simulated $002/00\bar{2}$ Kikuchi band in 160 nm thick, [110]-Si for zero loss and triple plasmon energy loss. The intensity profile was extracted from the box region in Figure 7e. The integrated intensity within the Kikuchi band was normalised for a direct visual comparison.

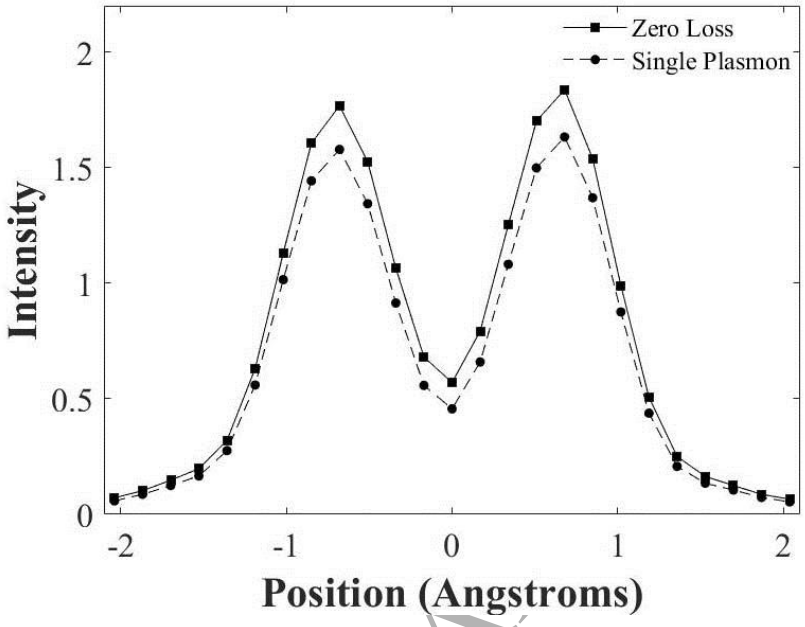

(a)

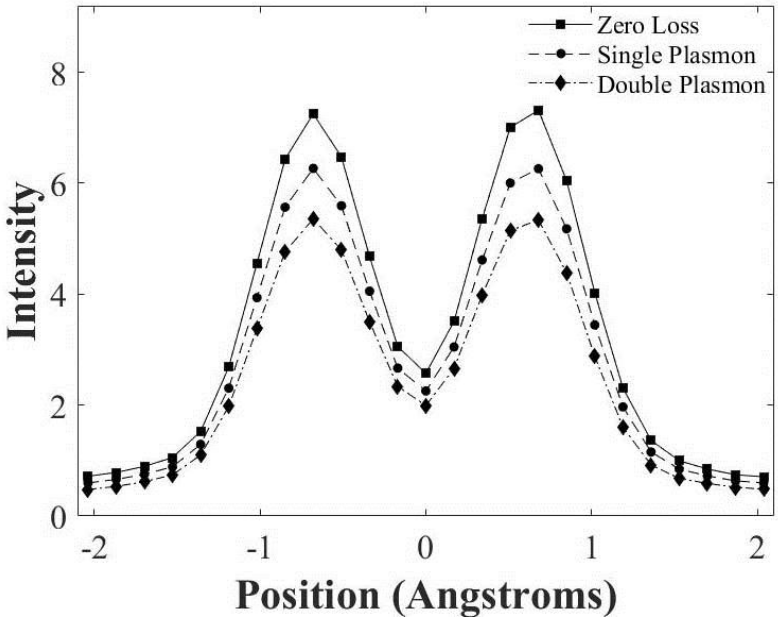

(b)

Figure 9: (a) Simulated HAADF intensity profiles across a 10 nm thick, [110]-Si specimen. An aberration free, 20 mrad semi-convergence angle probe at 200 kV was assumed in the simulation. Profiles are shown for 'zero loss' and single plasmon scattering events, and were obtained by incoherently summing the results from 50 supercell configurations. (b) is the

equivalent plot for a 50 nm thick, [110]-Si specimen with profiles for ‘zero loss’, single and double plasmon scattering superimposed.